nature physics

ARTICLES

https://doi.org/10.1038/s41567-019-0457-0

Symmetry-enforced chiral hinge states and surface quantum anomalous Hall effect in the magnetic axion insulator $Bi_{2-x}Sm_xSe_3$

Changming Yue[1,2], Yuanfeng Xu[1,2], Zhida Song[1,2], Hongming Weng[1,2,3,4,5], Yuan-Ming Lu[6], Chen Fang[1,3,4,5,7] and Xi Dai[8]*

The existence of topological hinge states is a key signature for a newly proposed class of topological matter, the second-order topological insulators. In the present paper, a universal mechanism to generate chiral hinge states in the ferromagnetic axion insulator phase is introduced, which leads to an exotic transport phenomenon, the quantum anomalous Hall effect (QAHE) on some particular surfaces determined by both the crystalline symmetry and the magnetization direction. A realistic material system, Sm-doped Bi_2Se_3, is then proposed to realize such exotic hinge states by combining first-principles calculations and Green's function techniques. A physically accessible way to manipulate the surface QAHE is also proposed, which makes it very different from the QAHE in ordinary 2D systems.

The bulk–boundary correspondence[1] is one of the most important physical consequences of topological matter. In most of the cases, the bulk–boundary correspondence refers to the existence of guaranteed gapless quasi-particle excitations on the $(d-1)$-dimensional boundary (with d being the dimension of the system), given that the symmetries required to protect such a topological state are still preserved on the boundary[2–6]. Very recently, a new type of bulk–boundary correspondence was proposed for a special class of topological materials called second-order topological insulators (SOTIs)[7–14], where the corresponding topological quasi-particle states appear in the $(d-2)$ instead of $(d-1)$-dimensional boundaries. In particular, non-trivial corner states (0D) will appear at the corners of a two-dimensional SOTI and helical/chiral hinge states (1D) will appear at some particular hinges of a three-dimensional SOTI. It is now understood that SOTI may be protected by different types of symmetries, such as rotation symmetries[11,12,14], mirror symmetries[6,10], inversion symmetry[14–17], nonsymmorphic symmetries and roto-reflection symmetries[18,19]. Some proposals for realizing SOTI have also emerged[13,20], and analogues of SOTI in superconductors[17,21] and even boson systems have attracted much attention[12,22,23].

Similar to the ordinary TI[5,24–26], the general definition of SOTI can be expressed as band insulators that can not be smoothly deformed to the atomic insulators[27–29] without symmetry breaking or closing the bulk energy gap. Unlike topological insulators, where each surface is gapless, a generic $(d-1)$-dimensional surface of d-dimensional SOTI is gapped and theoretically can be described by 2D Dirac equations with finite mass terms, which can be either positive or negative to open the gap. Then, on the entire boundary of a SOTI, there must be $(d-2)$-dimensional domain walls between surfaces having opposite masses, at which are located gapless topological modes. For the 2D SOTI, additional chiral or charge conjugation symmetry is required to protect the corner states[8], which is difficult to realize in materials. However, for 3D SOTI, the chiral or helical hinge states can be enforced by some bulk crystalline topological invariants (that is, the mirror Chern number (MCN) C_m), but protected by more general symmetries[12,14]. For example, for the helical hinge states, as first introduced in refs. [6,10], the existence of non-trivial hinge states can be enforced by the non-zero mirror Chern number $C_m=2N$ defined on some particular mirror-invariant planes, with N being an odd integer. The non-trivial helical states will persist even when the mirror symmetry is no longer present, and hence MCN cannot be defined. As long as both the bulk and surfaces around that particular hinge are all fully gapped, the only symmetry requirement to protect the non-trivial helical mode in such cases is the time-reversal symmetry. In ref. [10], SnTe with strain along the (100) direction is proposed to be the first realistic material that supports the non-trivial helical states on the hinge formed between (100) and (010) surfaces.

Compared to helical hinge states, chiral hinge states are even more stable, because no symmetry is required to protect them. Similar to the chiral edge states in 2D quantum Hall systems[4,30], the chiral hinge states associated with a specific surface will lead to the surface quantum anomalous Hall effect (QAHE)[31,32], which is the QAHE[33–36] on a surface of a three-dimensional object and has never been observed in DC transport before. In the present Letter, we will propose that both the chiral hinge states and hence the surface QAHE can be realized in ferromagnetic axion insulators. Although the concept of axion insulators was proposed much earlier, its relationship to SOTI with chiral hinge states has been discussed only very recently[37]. After that, we further propose a realistic material system, a Sm-doped Bi_2Se_3 single crystal, to realize such an axion insulator and SOTI with chiral hinge states. The high-quality single crystal of Sm-doped Bi_2Se_3 has been already obtained in ref. [38] with

[1]Beijing National Laboratory for Condensed Matter Physics and Institute of Physics, Chinese Academy of Sciences, Beijing, China. [2]University of Chinese Academy of Sciences, Beijing, China. [3]Songshan Lake Materials Laboratory, Dongguan, Guangdong, China. [4]CAS Centre for Excellence in Topological Quantum Computation, Beijing, China. [5]Physical Science Laboratory, Huairou National Comprehensive Science Center, Beijing, China. [6]Department of Physics, The Ohio State University, Columbus, OH, USA. [7]Kavli Institute for Theoretical Sciences, Chinese Academy of Sciences, Beijing, China. [8]Department of Physics, Hong Kong University of Science and Technology, Clear Water Bay, Kowloon, Hong Kong. *e-mail: daix@ust.hk

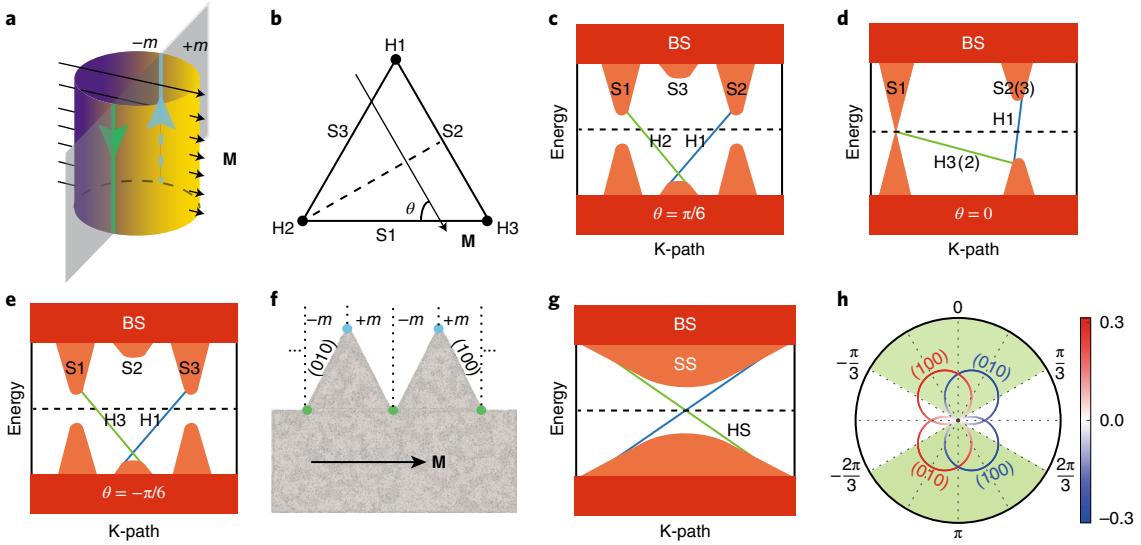

Fig. 1 | Schematic demonstration for the emergence of hinge states. a, Chiral hinge states emerge on the domain wall of the surface states with magnetic polarization applied perpendicular to the mirror plane. **b**–**e**, 3D TI with C_{3v} symmetry (**b**) and schematic illustration of the evolution of its surface states and hinge states with the magnetic polarization applied along different directions (**c**–**e**). **f**, Proposed configuration of the magnetically doped Bi_2Se_3 sample that can be adopted to detect the chiral hinge states. **g**, Schematic plot of the energy dispersion of the corresponding hinge states in **f**. **h**, Ratio $m/|\mathbf{M}|$ for (010) and (100) surface states as a function of the direction of magnetization, θ. The green shaded area denotes the range of θ where the hinge states are formed. For **a** and **c** to **g**, blue and green lines denote two hinge states with opposite chirality.

very low carrier density and Curie temperatures as high as 52 K. The easy axis of the magnetization has been confirmed experimentally to be within the *ab* plane. On the other hand, in quantum electrodynamics, Lorentz invariance allows, in addition to the Maxwell term, a topological term of the form $\frac{\theta}{4\pi}\mathbf{E}\cdot\mathbf{B}$, where the coupling strength θ is called the axion field[39]. A static θ is quantized to 0 or π in the presence of time-reversal symmetry[40], and $\theta = 0$ and π for trivial and topological insulators, respectively. It was then realized that in the absence of time-reversal, spatial symmetries can also quantize the value of θ, inducing a natural generalization of topological insulators[41]. In fact, as long as the spatial symmetry is improper (that is, it flips the orientation of the space), a uniform θ can take only 0 or π. Such spatial symmetries include inversion, mirror, S_4 and S_6. Therefore, in Sm-doped Bi_2Se_3, once the ferromagnetic order has been fully developed, the system has no time-reversal symmetry but still has inversion and mirror symmetries, which can quantize the θ angle to be 0 or π. Moreover, for such systems the θ angle can be determined easily by counting the number of occupied eigenstates with negative parity at the eight time-reversal-invariant momenta[42], according to which 3D insulators without time-reversal symmetry can be classified into normal insulator, axion insulator, 3D quantum Hall insulator or insulator with quantized polarization. From our density functional theory (DFT) calculations, the effective exchange field acting on the low-energy bands is around 20 meV, which is much smaller than the semiconductor gap in Bi_2Se_3 (around 0.3 eV), thus keeping the system within the axion insulator phase. We also checked that by changing the exchange field smoothly from zero to the actual value, the bulk gap remains open during the whole process, which confirms that the system is truly in the axion insulator phase. On the other hand, the parity and mirror eigenvalue for the occupied states obtained by our calculation imply that this material system can also be classified as a topological crystalline insulator with the 'strong index' being odd, as introduced in ref. [37], from which the 1D hinge state can also be inferred.

The presence of the chiral hinge states can be illustrated schematically in Fig. 1b. Since the crystal structure of Bi_2Se_3 contains three vertical mirror planes, one of them can survive the ferromagnetic order by setting the magnetization direction perpendicular to that mirror plane, as shown in Fig. 1b. The original Dirac surface states on different sides of the mirror plane (S1 and S3) will acquire finite masses, which have opposite signs forced by the mirror symmetry, as illustrated in Fig. 1b. Therefore, on hinge H2 between surface S1 and S3 in Fig. 1b, a domain wall between massive Dirac surface states with different mass signs is enforced by the mirror symmetry, leading to 1D chiral states on the corresponding hinge. Since the 1D chiral mode is stable against any weak perturbations, when the Zeeman field rotates away from the symmetric position and the system no longer has a mirror symmetry, the chiral hinge states cannot disappear immediately. However, its location can be modified or even moved from one hinge to another once the gap on surface S1 or S3 is closed and reopened, as illustrated schematically in Fig. 1c–e.

The above argument can be made more general. It is usually thought that at the boundary of a region with $\theta = \pi$, there are gapless 2D surface states, which are nothing but the single Dirac fermion in the case of topological insulators. However, if the symmetry quantizing θ is a spatial symmetry, which is the case for the FM axion insulators, the 2D surface states exist only if the interface preserves the symmetry, and on a surface where it is broken, a mass gap generically exists. This leads to another interesting possibility: the mass is forced to change signs on the entire boundary of the topological state, creating domain walls of mass gaps[43], because either the mirror reflection or the inversion symmetry flips the sign of the mass terms for the surface Dirac Hamiltonian. Along any one of these domain walls, there are 1D chiral modes (that is, the $(d-2)$-dimensional topological edge states), the recently discovered boundary manifestation of the non-trivial topology in the bulk in the absence of gapless surface states. In Fig. 1a, we illustrate the 1D chiral modes on the surface of 3D axion insulators protected by the improper symmetry—mirror reflection in this case.

To calculate the hinge states, we adopt an approximation where the low-energy physics of Sm-doped Bi_2Se_3 can be modelled by the tight-binding Hamiltonian for the pure Bi_2Se_3 together with a magnetic exchange field acting on the *p* orbitals of both the Bi and

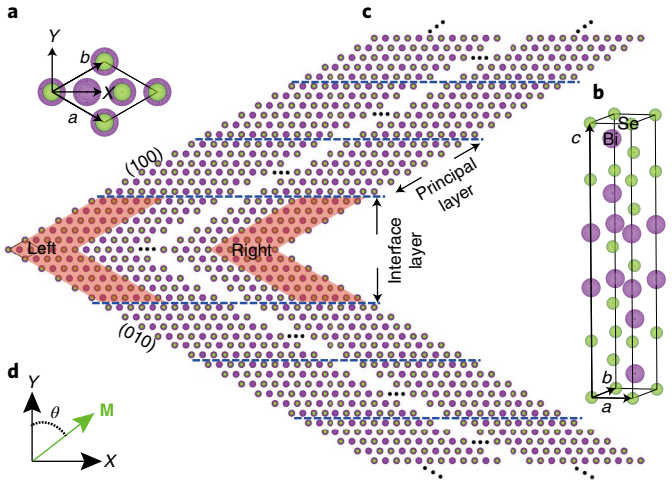

Fig. 2 | The structure proposed for the calculation of the hinge states. **a**,**b**, Crystal structure of Bi_2Se_3. *X*, *Y* and *Z* form the global right-handed coordinate system. **c**, The bi-semi-infinite open boundary geometry in which the (010) and (100) surfaces meet at the Left and Right hinges parallel to the *c* direction. The structure is semi-infinite along the *a* and *b* directions, periodic along the *c* direction and finite along the *X* direction. The length in the *X* direction is 20 lattice constants. Principal layer (PL) is a group of atomic layers that is large enough such that only adjacent PLs interact. Interface layer is a group of atomic layers located between the two semi-infinite parts. Generally, the interface layer is composed of the first PL along the *a* direction combined with the first PL along the *b* direction. **d**, The easy direction of the magnetization **M** lies in the *ab* plane, with θ the angle between **M** and the *y* axis.

Table 1 | Local right-handed coordinate system $\mathbf{e}_{x,y,z}$, velocity v and g-factor g of (010) and (100) surfaces, respectively.

	(010)			(100)		
$\mathbf{e}_x$	$\frac{\sqrt{3}}{2}$	$-\frac{1}{2}$	0	$-\frac{\sqrt{3}}{2}$	$-\frac{1}{2}$	0
$\mathbf{e}_y$	0	0	1	0	0	1
$\mathbf{e}_z$	$-\frac{1}{2}$	$-\frac{\sqrt{3}}{2}$	0	$-\frac{1}{2}$	$\frac{\sqrt{3}}{2}$	0
$\mathbf{v}_x$	0	0.4316	0.4951	0	0.4316	0.4951
$\mathbf{v}_y$	−0.7649	0	0	−0.7649	0	0
$\mathbf{g}_x$	0.7782	0	0	0.7782	0	0
$\mathbf{g}_y$	0	0.5354	−0.0957	0	0.5354	−0.0957
$\mathbf{g}_z$	0	0	0.4778	0	0	0.4778

Entries of local $\mathbf{e}_{x,y,z}$ are given in terms of unit vectors of the global coordinate system *x*, *y*, *z* shown in Fig. 2a. The unit of **v** is eV Å and the unit of **g** is eV^{-1}.

Se atoms. Moreover, we generalize the recursive Green's function method[44], which is widely used for the spectral functions of the surface or interface states, to calculate the hinge states for the SOTI (details given in the final section of Methods). As shown in Fig. 2c, two hinges (labelled as Left and Right, respectively) are generated by joining two semi-infinite slabs along different directions, namely [1,0,0] and [0,1,0]. The hinge area can then be viewed as the left and right ends of the interface region between the two slabs oriented along different directions, with the cross-section perpendicular to the *c* axis. The projected spectral functions for the two hinge regions can then be obtained by following the standard procedures of the recursive Green's function method[44].

As already confirmed experimentally[38], in $Sm_xBi_{2-x}Se_3$ the magnetic moments on Sm ions ordered ferromagnetically under $T_c \approx 52$ K. The easy axis lies within the *ab* plane and can be easily tuned by a small external magnetic field. The crystal structure of Bi_2Se_3 contains three vertical mirror planes and will survive the ferromagnetic order if the magnetization **M** is along the [−1, 1, 0], [0, −1, 0] and [1, 0, 0] directions, respectively (corresponding to $\theta = 0$, $2\pi/3$ and $4\pi/3$ in Fig. 1b, respectively). Then, as we discussed above, the existence of the mirror symmetry in the axion insulator will force the mass terms on different sides of the mirror-symmetric hinge to be opposite in sign, which guarantees the existence of the chiral hinge states centred at that particular hinge. Interestingly, since the chiral hinge states are topologically stable, the breaking of the corresponding mirror symmetry (that is, by rotating the magnetization **M** away from the particular angle mentioned above), the chiral hinge states do not disappear immediately. In fact it will disappear only when the surface gap closes on either of the two nearby surfaces. Otherwise, as long as the gap still exists on both surfaces near the hinge, the domain wall feature still remains and the only effect of the mirror-symmetry breaking is to modify the wavefunction of the hinge state to be asymmetric about the mirror plane.

The local spectral functions at both the left and right hinges can be obtained by projecting the imaginary part of the Green's function to the corresponding hinge area, which can be expressed as $\rho_{L/R}(k_z,\omega) = -1\pi \sum_{i\in L/R} \mathrm{Im}G_{ii}(k_z,\omega)$, where the hinge area L and R are illustrated by the orange colour shaded block Left and Right in Fig. 2c, respectively. Then the hinge spectral functions can be obtained by applying the recursive Green's function method introduced above. Alternatively the existence of chiral hinge modes can be inferred from checking the mass terms on the nearby surfaces, whose Hamiltonian can be written as

$$H_{SF} = \mathbf{v}_x \cdot \boldsymbol{\sigma} k_x + \mathbf{v}_y \cdot \boldsymbol{\sigma} k_y + \mathbf{g}_x \cdot \boldsymbol{\sigma} M_x + \mathbf{g}_y \cdot \boldsymbol{\sigma} M_y + \mathbf{g}_z \cdot \sigma M_z \quad (1)$$

where *x*, *y*, *z* form the local right-handed coordinate system and $\mathbf{v}_i$, $\mathbf{g}_i$ are vectors defined in pseudo-spin space. Both the velocity and g-factor vectors for the (100) and (010) surfaces of $Sm_xBi_{2-x}Se_3$ can be obtained by the corresponding surface calculations based on the effective tight-binding Hamiltonian with their values listed in Table 1.

Then the mass associated with that particular surface Dirac equation can be expressed as

$$m = \frac{(\mathbf{v}_x \times \mathbf{v}_y) \cdot (\mathbf{g}_x M_x + \mathbf{g}_y M_y + \mathbf{g}_z M_z)}{|\mathbf{v}_x \times \mathbf{v}_y|} \quad (2)$$

Bearing in mind the fact that the magnetization lies in the *ab* plane and using velocity *v* and g-factor *g* listed in Table 1, we can express *m* as a function of the magnetization direction θ as $m_{010} = -0.3140|\mathbf{M}|\sin(\theta + \pi/3)$ and $m_{100} = -0.3410|\mathbf{M}|\sin(\theta - \pi/3)$, which are plotted in Fig. 1h. Please note that the dimension of the quantity *m* in the above equation is energy.

The mass term vanishes at $\theta = \pi/3$ for the (100) surface and $\theta = 2\pi/3$ for the (010) surface, indicating the surface topological transitions at these two angles, after which the hinge states moved from one hinge to another. As we discussed above, the chiral hinge states can exist only when the two nearby surfaces have mass terms with opposite signs, as indicated by the green area in Fig. 1h.

In the Fig. 3a–d, we plot the hinge spectral functions calculated by the recursive Green's function method for four typical magnetization directions: 0, $\pi/6$, $\pi/3$ and $\pi/2$. In Fig. 3a, the magnetization is along the *Y* direction, which preserves the *XZ* mirror plane. As we discussed above, the mirror symmetry guarantees the sign change for the mass terms on the nearby surfaces leading to chiral hinge states. The energy dispersion of the hinge states on both left and right hinges can be found by checking the spectral functions

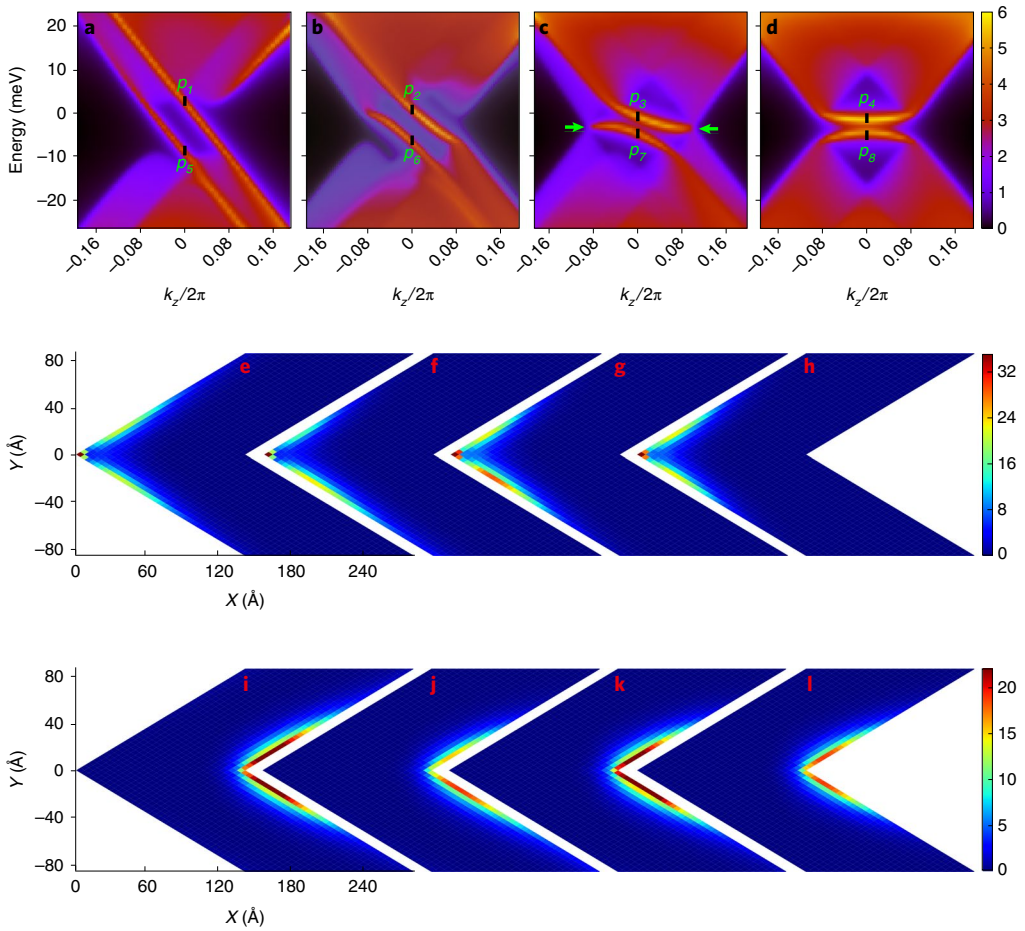

Fig. 3 | The projected spectral functions on the interface layer and their spatial distribution. a–d, Projected spectral functions as **M** is rotated from $\theta=0$ to $\theta=\pi/6$, $\theta=\pi/3$ and $\theta=\pi/2$, respectively. Points $\{p_1, \ldots, p_8\}$, with $k_z=0$, are labelled to show the spatial distribution of these points in **e** to **l**. **e–h**, Spatial distribution of the spectral functions at p_1 to p_4 labelled in **a** to **d**, showing the spatially localized states distributed around the left hinge. **i–l**, Spatial distribution of spectral functions at p_5 to p_8 labelled in **a** to **d**, showing the spatially localized states distributed around the right hinge.

projected to the whole interface area, which are plotted in Fig. 3a. Clear chiral hinge states can be found with a similar velocity around $-1.60\times10^5\,\mathrm{m\,s^{-1}}$. As shown in Fig. 3e,i, the spatial distribution functions for the peaks marked as p_1 and p_5 in Fig. 3a are centred at the left and right hinges, respectively, which are fully symmetric around the corresponding hinge due to the mirror symmetry. Combined with Fig. 3a,e,i, we know that the left and right hinge states all disperse positively along the c direction. Further examination of the spatial distribution of the spectral weight confirms that the chiral hinge mode on each particular hinge smoothly connects the valence bands on the (100) surface and the conduction bands on the (010) surface. As the magnetization angle θ is rotated clockwise away from zero, the surface gap on (100) is getting smaller quickly and the hinge states are still there with a slightly modified velocity and an asymmetric spatial distribution around the hinge, as shown in Fig. 3f. When the magnetization angle θ becomes $\pi/3$, the gap on (100) surface closes completely, forming surface Dirac cones on the corresponding surfaces, as indicated by the two arrows in Fig. 3c, which shows the topological phase transition on these surfaces. After the transition the connection pattern of the hinge states changed completely, as shown in Fig. 3d, the hinge states now connect within the conduction (label p_4) or the valence bands (label p_8) on (100) and (010) surfaces and become topologically trivial.

The existence of chiral hinge modes will cause the QAHE on the surfaces of the $Sm_xBi_{2-x}Se_3$. The experimental set-up can be schematically plotted in Fig. 1f. By cutting the $Sm_xBi_{2-x}Se_3$ single crystal using the focused ion beam technique to obtain the zig–zag surface structure formed by (100) and (010) surfaces, the counter propagating chiral hinge modes can then be induced by the horizontal magnetization on the 'ridge' and 'valley' area, as shown in Fig. 1g. After putting leads on both ridges and valleys, the surface QAHE can be detected by standard DC measurements for the Hall effect. In principle, we need a bulk insulating sample for the actual detection of the surface QAHE. However, we do not need the carrier density to reach zero to fulfill the above condition. For systems with a disorder potential, the bulk conductivity will vanish at zero temperature when the chemical potential is below the mobility gap. Therefore we should have the chance to detect surface QAHE at a low enough temperature for a disordered sample, just like the situation in Cr-doped Bi_2Te_3 thin film, where the QAHE has been observed[33,34]. In fact, bulk insulating samples have been achieved in similar materials already[45] and experimental evidence of surface gaps has also been found in some of the related systems as well[46]. Therefore, we expect the proposed surface QAHE to be feasible in the high-quality samples of this system. There is another type of experiment that can demonstrate the existence of the chiral hinge state. We only need to put two leads on one of the ridge or valleys of the above-mentioned structure and the chiral hinge states will contribute to 'non-reciprocal' DC transport, which manifests itself as the difference of the DC resistance for voltages applied parallel or anti-parallel to the hinge. Since the bulk and surface contribution of the conductivity is always reciprocal, this type of experiment is

easier than the DC measurement of QAHE and works even for non-zero bulk and surface conductivity.

In conclusion, we proposed in the paper that the Sm-doped Bi_2Se_3 single crystal is a magnetic axion insulator and provides an ideal material platform to realize helical hinge states on the particular hinges of the crystals. Such nontrivial hinge states demonstrate that the magnetic axion insulator can also be viewed as higher-order topological insulators with the new type of bulk–boundary correspondence described in the paper. The surface QAHE is the most striking observable effect caused by the chiral hinge states in the Sm-doped Bi_2Se_3 single crystal.

Online content

Any methods, additional references, Nature Research reporting summaries, source data, statements of data availability and associated accession codes are available at https://doi.org/10.1038/s41567-019-0457-0.

Received: 3 July 2018; Accepted: 5 February 2019;
Published online: 18 March 2019

References

1. Ryu, S. et al. Topological origin of zero-energy edge states in particle–hole symmetric systems. *Phys. Rev. Lett.* **89**, 077002 (2002).
2. Fu, L. Topological crystalline insulators. *Phys. Rev. Lett.* **106**, 106802 (2011).
3. Wang, Z. et al. Hourglass fermions. *Nature* **532**, 189–194 (2016).
4. Hatsugai, Y. Chern number and edge states in the integer quantum Hall effect. *Phys. Rev. Lett.* **71**, 3697–3700 (1993).
5. Kane, C. L. et al. Z_2 topological order and the quantum spin Hall effect. *Phys. Rev. Lett.* **95**, 146802 (2005).
6. Hsieh, T. H. et al. Topological crystalline insulators in the SnTe material class. *Nat. Commun.* **3**, 982 (2012).
7. Benalcazar, W. A. et al. Electric multipole moments, topological multipole moment pumping, and chiral hinge states in crystalline insulators. *Phys. Rev. B* **96**, 245115 (2017).
8. Langbehn, J. et al. Reflection-symmetric second-order topological insulators and superconductors. *Phys. Rev. Lett.* **119**, 246401 (2017).
9. Ezawa, M. Magnetic second-order topological insulators and semimetals. *Phys. Rev. B* **97**, 155305 (2018).
10. Schindler, Frank et al. Higher-order topological insulators. *Sci. Adv.* **4**, eaat0346 (2018).
11. Benalcazar, W. A. et al. Quantized electric multipole insulators. *Science* **357**, 61–66 (2017).
12. Song, Z. et al. $(d-2)$-dimensional edge states of rotation symmetry protected topological states. *Phys. Rev. Lett.* **119**, 246402 (2017).
13. Schindler, F. et al. Higher-order topology in bismuth. *Nat. Phys.* **14**, 918–924 (2018).
14. Fang, C. et al. Rotation anomaly and topological crystalline insulators. Preprint at https://arxiv.org/abs/1709.01929 (2017).
15. Ari, M. T. et al. Entanglement and inversion symmetry in topological insulators. *Phys. Rev. B* **82**, 241102(R) (2012).
16. Taylor, L. H. et al. Inversion-symmetric topological insulators. *Phys. Rev. B* **83**, 245132 (2011).
17. Eslam, K. Higher-order topological insulators and superconductors protected by inversion symmetry. *Phys. Rev. B* **97**, 205136 (2018).
18. Zhida, S. et al. Quantitative mappings between symmetry and topology in solids. *Nat. Commun.* **9**, 3530 (2018).
19. Eslam, K. et al. Symmetry indicators and anomalous surface states of topological crystalline insulators. *Phys. Rev. X* **8**, 031070 (2018).
20. Xiaoting, Z. et al. Topological crystalline insulator states in the Ca_2As family. *Phys. Rev. B* **98**, 241104 (2018).
21. Hassan, S. et al. Topological crystalline superconductivity and second-order topological superconductivity in nodal-loop materials. *Phys. Rev. B* **97**, 094508 (2018).
22. Yizhi, Y. et al. Higher order symmetry-protected topological states for interacting bosons and fermions. *Phys. Rev. B* **98**, 235102 (2018).
23. Sheng-Jie, H. et al. Building crystalline topological phases from lower-dimensional states. *Phy. Rev. B* **96**, 205106 (2017).
24. Hasan, M. Z. et al. Colloquium: topological insulators. *Rev. Mod. Phys.* **82**, 3045–3067 (2010).
25. Qi, X.-L. et al. Topological insulators and superconductors. *Rev. Mod. Phys.* **83**, 1057–1110 (2011).
26. Yoichi, A. et al. Topological crystalline insulators and topological superconductors: from concepts to materials. *Ann. Rev. Cond. Mat. Phys.* **6**, 361–381 (2015).
27. Po, H. C. et al. Complete theory of symmetry-based indicators of band topology. *Nat. Commun.* **8**, 50 (2017).
28. Bradlyn, B. et al. Topological quantum chemistry. *Nature* **547**, 298–305 (2017).
29. Soluyanov, A. A. et al. Wannier representation of topological insulators. *Phys. Rev. B* **83**, 035108 (2011).
30. Klitzing, K. V. et al. New method for high-accuracy determination of the fine-structure constant based on quantized Hall resistance. *Phys. Rev. Lett.* **45**, 494–497 (1980).
31. Mong, R. S. K. et al. Antiferromagnetic topological insulators. *Phys. Rev. B* **81**, 245209 (2010).
32. Nomura, K. et al. Surface-quantized anomalous Hall current and the magnetoelectric effect in magnetically disordered topological insulators. *Phys. Rev. Lett.* **106**, 166802 (2011).
33. Yu, R. et al. Quantized anomalous Hall effect in magnetic topological insulators. *Science* **329**, 61–64 (2010).
34. Chang, C.-Z. et al. Experimental observation of the quantum anomalous Hall effect in a magnetic topological insulator. *Science* **340**, 167–170 (2013).
35. Haldane, F. D. M. Model for a quantum hall effect without Landau levels: condensed-matter realization of the 'parity anomaly'. *Phys. Rev. Lett* **61**, 2015–2018 (1988).
36. Liang, Wu et al. Quantized Faraday and Kerr rotation and axion electrodynamics of a 3d topological insulator. *Science* **354**, 1124–1127 (2016).
37. Luka, T. et al. Higher-order bulk-boundary correspondence for topological crystalline phases. *Phys. Rev. X* **9**, 011012 (2019).
38. Chen, T. et al. High-mobility Sm-doped Bi_2Se_3 ferromagnetic topological insulators and robust exchange coupling. *Adv. Mater.* **27**, 4819–4823 (2015).
39. Wilczek, F. Two applications of axion electrodynamics. *Phys. Rev. Lett.* **58**, 1799–1802 (1987).
40. Qi, X.-L. et al. Topological field theory of time-reversal invariant insulators. *Phys. Rev. B* **78**, 195424 (2008).
41. Essin, A. M. et al. Magnetoelectric polarizability and axion electrodynamics in crystalline insulators. *Phys. Rev. Lett.* **102**, 146805 (2009).
42. Ari, M. T. et al. Quantized response and topology of magnetic insulators with inversion symmetry. *Phys. Rev. B* **85**, 165120 (2012).
43. Zhang, F. et al. Surface state magnetization and chiral edge states on topological insulators. *Phys. Rev. Lett.* **110**, 046404 (2013).
44. Sancho., M. P. L. et al. Highly convergent schemes for the calculation of bulk and surface Green functions. *J. Phys. F* **15**, 851 (1985).
45. Zhi, R. et al. Large bulk resistivity and surface quantum oscillations in the topological insulator Bi_2Te_2Se. *Phys. Rev. B* **82**, 241306 (2010).
46. Chen, Y. L. et al. Massive Dirac fermion on the surface of a magnetically doped topological insulator. *Science* **329**, 659–662 (2010).

Acknowledgements

We thank B.A. Bernevig and T. Neupert for helpful discussions. X.D., C.F. and H.M.W. are supported by the Ministry of Science and Technology of China (grant no. 2016YFA0300600) and the K.C. Wong Education Foundation (grant no. GJTD-2018-01). X.D. acknowledges financial support from the Hong Kong Research Grants Council (project no. GRF16300918). C.F. acknowledges financial support from the Ministry of Science and Technology of China (grant no. 2016YFA0302400), the Natural Science Foundation of China (grant no. 11674370), the Chinese Academy of Sciences (no. XXH13506-202, XDB28000000), the Beijing Municipal Science & Technology Commission (no. Z181100004218001) and the Beijing Natural Science Foundation (no. Z180008). H.M.W. is also supported by the Ministry of Science and Technology of China (grant no. 2018YFA0305700), the National Natural Science Foundation (grant no. 11674369) and the Science Challenge Project (no. TZ2016004). Y.-M.L. acknowledges the NSF under award number DMR-1653769.

Author contributions

C.F., Y.M.L. and X.D. developed the theory and designed the research. C.M.Y. carried out the numerical calculations for the hinge states. Y.F.X. and H.M.W. did the calculations for the effective exchange field. Z.D.S. did the symmetry analyses for the numerical results. All authors contributed to the writing of the manuscript.

Competing interests

The authors declare no competing interests.

Additional information

Supplementary information is available for this paper at https://doi.org/10.1038/s41567-019-0457-0.

Reprints and permissions information is available at www.nature.com/reprints.

Correspondence and requests for materials should be addressed to X.D.

Journal peer review information: *Nature Physics* thanks Minoru Kawamura, Titus Neupert and other anonymous reviewer(s) for their contribution to the peer review of this work.

Publisher's note: Springer Nature remains neutral with regard to jurisdictional claims in published maps and institutional affiliations.

Methods

Calculation of effective magnetic exchange field. Recently, Sm-doped Bi_2Se_3 magnetic topological insulators have been experimentally realized[38] with the Curie temperature being about 52 K. We have simulated this system theoretically by first-principles methods using the VASP package[47–49]. In the calculation, a $2\times2\times1$ supercell structure of Bi_2Se_3 is constructed with one Bi atom being replaced by a Sm atom. In such a $SmBi_{23}Se_{36}$ system, Sm^{3+} is in the high-spin state and its total magnetization strength is as large as $5.4\mu_B$. A very dense momentum and energy grid is adopted to calculate the spin-polarized density of states of Bi and Se, which are shown in Supplementary Fig. 1. The exchange field splitting ΔE of the p orbitals can be roughly estimated by equation (3), which are about 20 meV and 10 meV for p orbitals on Se and Bi, respectively.

$$\Delta E=\frac{\int\varepsilon\rho_{\downarrow}(\varepsilon)\mathrm{d}\varepsilon}{\int\rho_{\downarrow}(\varepsilon)\mathrm{d}\varepsilon}-\frac{\int\varepsilon\rho_{\uparrow}(\varepsilon)\mathrm{d}\varepsilon}{\int\rho_{\uparrow}(\varepsilon)\mathrm{d}\varepsilon} \tag{3}$$

where $\rho_{\downarrow(\uparrow)}(\varepsilon)$ is the density of states of the majority(minority) spin component of p orbitals.

Recursive Green function method in the calculation of hinge states. To carry out realistic calculations for the hinge states, we design a bi-semi-infinite open boundary geometry (as shown in Supplementary Fig. 2) in which the (010) and (100) surfaces meet at Left and Right hinges parallel to the c direction. The geometry is semi-infinite along the a and b directions, periodic along the c direction, and finite along the x direction. The size along the x direction is 20 unit cells in the realistic calculation, ensuring negligible finite-size effects arising from hybridization between left and right hinges. Principal layer (PL) is a group of atomic layers that is large enough such that only adjacent PLs interact. Division of ULs and LLs into PLs is a common strategy to express the Hamiltonian in the block tridiagonal form

$$H=\begin{pmatrix}
H_{II} & H_{IR_0} & H_{IR_{\bar{0}}} & 0 & \cdots & & & & & \\
H_{IR_0}^{\dagger} & H_{R_0R_0} & 0 & H_{R_0R_1} & 0 & \cdots & & & & \\
H_{IR_{\bar{0}}}^{\dagger} & 0 & H_{R_{\bar{0}}R_{\bar{0}}} & 0 & H_{R_{\bar{0}}R_{\bar{1}}} & 0 & \cdots & & & \\
0 & H_{R_0R_1}^{\dagger} & 0 & H_{R_1R_1} & 0 & H_{R_1R_2} & 0 & \cdots & & \\
\vdots & 0 & H_{R_{\bar{0}}R_{\bar{1}}}^{\dagger} & 0 & H_{R_{\bar{1}}R_{\bar{1}}} & 0 & H_{R_{\bar{1}}R_{\bar{2}}} & 0 & \cdots & \\
 & \vdots & 0 & H_{R_1R_2}^{\dagger} & 0 & H_{R_2R_2} & 0 & H_{R_2R_3} & 0 & \cdots \\
 & & \vdots & 0 & H_{R_{\bar{1}}R_{\bar{2}}}^{\dagger} & 0 & H_{R_{\bar{2}}R_{\bar{2}}} & 0 & H_{R_{\bar{2}}R_{\bar{3}}} & \ddots \\
 & & & \vdots & \ddots & \ddots & \ddots & \ddots & \ddots & \ddots
\end{pmatrix} \tag{4}$$

where the diagonal block $H_{R_iR_i}=H_{R_0R_0}$, $H_{R_{\bar{i}}R_{\bar{i}}}=H_{R_{\bar{0}}R_{\bar{0}}}$ and the hopping matrix $H_{R_iR_{i+1}}=H_{R_0R_1}$, $H_{R_{\bar{i}}R_{\bar{i+1}}}=H_{R_{\bar{0}}R_{\bar{1}}}$. Implicitly, each block of H is a function of momentum k_z, that is $H_{ij}\equiv H_{ij}(k_z)$. The tight-binding Hamiltonian is obtained from the maximally localized Wannier functions constructed by the wannier90[50] package interfaced to VASP[47–49]. Furthermore, Zeeman terms $H_z=\mathbf{M}\cdot\boldsymbol{\sigma}$ with the strength obtained from the first-principles calculations mentioned in the previous section are added to all p orbitals to simulate the ferromagnetic order arising from Sm doping.

For simplification, H_{IR} is used to denote hoppings between the interface layer and ULs, LLs:

$$H_{IR}\equiv\begin{pmatrix}H_{IR_0} & H_{IR_{\bar{0}}} & 0 & \cdots\end{pmatrix} \tag{5}$$

H_P, in block tridiagonal form, is to denote the Hamiltonian of ULs,

$$H_P\equiv\begin{pmatrix}
H_{R_0R_0} & H_{R_0R_1} & 0 & & \\
H_{R_0R_0}^{\dagger} & H_{R_0R_0} & H_{R_0R_1} & 0 & \\
0 & H_{R_0R_0}^{\dagger} & H_{R_0R_0} & H_{R_0R_1} & \ddots \\
 & \ddots & \ddots & \ddots & \ddots
\end{pmatrix} \tag{6}$$

and H_N, also in block tridiagonal form, is to denote the Hamiltonian of LLs

$$H_N\equiv\begin{pmatrix}
H_{R_{\bar{0}}R_{\bar{0}}} & H_{R_{\bar{0}}R_{\bar{1}}} & 0 & & \\
H_{R_{\bar{0}}R_{\bar{1}}}^{\dagger} & H_{R_{\bar{0}}R_{\bar{0}}} & H_{R_{\bar{0}}R_{\bar{1}}} & 0 & \\
0 & H_{R_{\bar{0}}R_{\bar{1}}}^{\dagger} & H_{R_{\bar{0}}R_{\bar{0}}} & H_{R_{\bar{0}}R_{\bar{1}}} & \ddots \\
 & \ddots & \ddots & \ddots & \ddots
\end{pmatrix} \tag{7}$$

Furthermore, we introduce a new 'direct sum' operation $\widetilde{\oplus}$ of two square matrices A and B as

$$A\,\widetilde{\oplus}\,B=\begin{pmatrix}
A_{11} & 0 & A_{12} & 0 & \cdots \\
0 & B_{11} & 0 & B_{12} & \cdots \\
A_{21} & 0 & A_{22} & 0 & \cdots \\
0 & B_{21} & 0 & B_{22} & \cdots \\
\vdots & \vdots & \vdots & \vdots & \ddots
\end{pmatrix} \tag{8}$$

Now we have

$$H\equiv\begin{pmatrix}H_{II} & H_{IR} \\ H_{IR}^{\dagger} & H_{RR}\end{pmatrix} \tag{9}$$

where

$$H_{RR}\equiv H_P\,\widetilde{\oplus}\,H_N \tag{10}$$

indicating that ULs and LLs are totally decoupled from each other.

The imaginary part of the interface Green function $G_{II}(k_z,\omega)$ can be written as

$$A_{II}(k_z,\omega)=-\frac{1}{\pi}\Im G_{II}(k_z,\omega) \tag{11}$$

$$G\equiv\begin{pmatrix}G_{II} & G_{IR} \\ G_{IR}^{\dagger} & G_{RR}\end{pmatrix} \tag{12}$$

$$(\omega+i\eta-H)G=1 \tag{13}$$

$$G_{II}(k_z,\omega+i\eta)=[(\omega+i\eta)-H_{II}-\Sigma_R]^{-1} \tag{14}$$

where Σ_R is the self-energy depicting comprehensive interactions between interface layer and ULs, LLs. Within the approximation of PL, Σ_R has a simple form as

$$\Sigma_R=H_{IR}g_{RR}H_{IR}^{\dagger}\approx H_{IR_0}g_{R_0R_0}H_{IR_0}^{\dagger}+H_{IR_{\bar{0}}}g_{R_{\bar{0}}R_{\bar{0}}}H_{IR_{\bar{0}}}^{\dagger} \tag{15}$$

where $g_{R_0R_0}$ and $g_{R_{\bar{0}}R_{\bar{0}}}$ are the 'surface' Green functions of ULs and LLs, respectively. Because H_P and H_N are all in triangular diagonal form, $g_{R_0R_0}$ and $g_{R_{\bar{0}}R_{\bar{0}}}$ can be solved by the standard recursive schemes[44]. Using equations (15, 14, 11), we obtain the spectral functions for the interface layer. A_{II} is a square matrix with its indices being the number of orbitals in the interface layer. The trace of A_{II} gives the integrated spectral shown in the first row of Fig. 3.

Data availability

The data that support the findings of this study are available from the corresponding authors upon reasonable request.

References

47. Kresse, G. et al. Ab initio molecular dynamics for liquid metals. *Phys. Rev. B* **47**, 558–561 (1993).
48. Kresse, G. et al. Efficiency of ab-initio total energy calculations for metals and semiconductors using a plane-wave basis set. *Comput. Mater. Sci* **6**, 15–50 (1996).
49. Kresse, G. et al. Efficient iterative schemes for ab initio total-energy calculations using a plane-wave basis set. *Phys. Rev. B* **54**, 11169–11186 (1996).
50. Arash, A. M. et al. An updated version of wannier90: a tool for obtaining maximally-localized Wannier functions. *Com. Phys. Comm.* **185**, 2309–2310 (2014).